Disentangling the temporal dynamics of nonthermal electrons in photoexcited gold nanostructures

Patrick O'Keeffe Daniele Catone Lorenzo Di Mario Francesco Toschi Michele Magnozzi Francesco Bisio Alessandro Alabastri Remo Proietti Zaccaria Andrea Toma Giuseppe Della Valle Alessandra Paladini**

Dr. P. O'Keeffe, Dr. F. Toschi, Dr. A. Paladini
Istituto di Struttura della Materia-CNR (ISM-CNR), Division of Ultrafast Processes in Materials (FLASHit), Area della Ricerca di Roma 1, 00015 Monterotondo Scalo, Italy.
Email Address: alessandra.paladini@cnr.it
Dr. D. Catone, Dr. L. Di Mario
Istituto di Struttura della Materia-CNR (ISM-CNR), Division of Ultrafast Processes in Materials (FLASHit), Area della Ricerca di Roma 2 Tor Vergata, Via del Fosso del Cavaliere 100, 00133 Rome, Italy.
Dr. M. Magnozzi
OptMatLab, Dip.to di Fisica, Università di Genova, via Dodecaneso 33, 16146 Genova, Italy.
Dr. F. Bisio
CNR-SPIN, Corso Perrone 24, 16152 Genova, Italy.
Dr. A. Alabastri
Department of Electrical and Computer Engineering, Rice University, 6100 Main Street, Houston, TX 77005, USA.
Dr. R. Proietti Zaccaria
Istituto Italiano di Tecnologia, Via Morego 30, 16163 Genova, Italy.
Dr. A. Toma
Istituto Italiano di Tecnologia, Via Morego 30, 16163 Genova, Italy.
Dr. G. Della Valle
Dip.to di Fisica, Politecnico di Milano, Piazza L. da Vinci 32, 20133, Milan, Italy.
Email Address: giuseppe.dellavalle@polimi.it

Keywords: *nonthermal electrons, ultrafast spectroscopy, transient absorbance, plasmonics, nanostructure*

The study of nonthermal electrons, generated upon photoexcitation of plasmonic nanostructures, plays a key role in a variety of contexts, from photocatalysis and energy conversion to photodetection and nonlinear optics. Their ultrafast relaxation and subsequent release of energy to a low energy distribution of thermalized *hot* electrons has been the subject of a myriad of papers, mostly based on femtosecond transient absorption spectroscopy (FTAS). However, the FTAS signal stems from a complex interplay of different contributions arising from both nonthermal and thermal electrons, making the disentanglement of the two a very challenging task, so far accomplished only in terms of numerical simulations. Here a combined approach is introduced, based on a post-processing of the FTAS measurements guided by a reduced semiclassical model, the so-called Extended Two-Temperature Model, which has allowed the purely nonthermal contribution to the pump-probe experimental map recorded for 2D arrays of gold nanoellipsoids to be isolated. This approach displays the intimate correlation between electron energy and probe photon energy on the ultrafast time-scale of electron thermalization. It also sheds new light on the ultrafast transient optical response of gold nanostructures, and will help the development of optimized plasmonic configurations for nonthermal electrons generation and harvesting.

1 Introduction

The generation of excited electrons in plasmonic nanostructures has attracted a great deal of attention in recent years mainly due to increasing interest in harvesting these electrons for purposes such as photocatalysis, photodetection, energy conversion and nanophotonics.[1, 2, 3, 4, 5, 6, 7] These electrons can be transferred into the electronic states of molecules close to the surface of the plasmonic nanostructures, and thus induce chemical reactions which would otherwise be energetically demanding.[8, 9, 10] They can also be injected into the conduction band of a semiconductor for use in photovoltaics,[11, 12, 13] photodetectors,[14, 15] and photoelectrochemical systems.[13, 16]
Upon excitation, energetic electrons are produced in a nonthermal distribution, i.e. the electron energies are skewed to high energies not describable by even a high temperature Fermi-Dirac distribution. [17, 18]

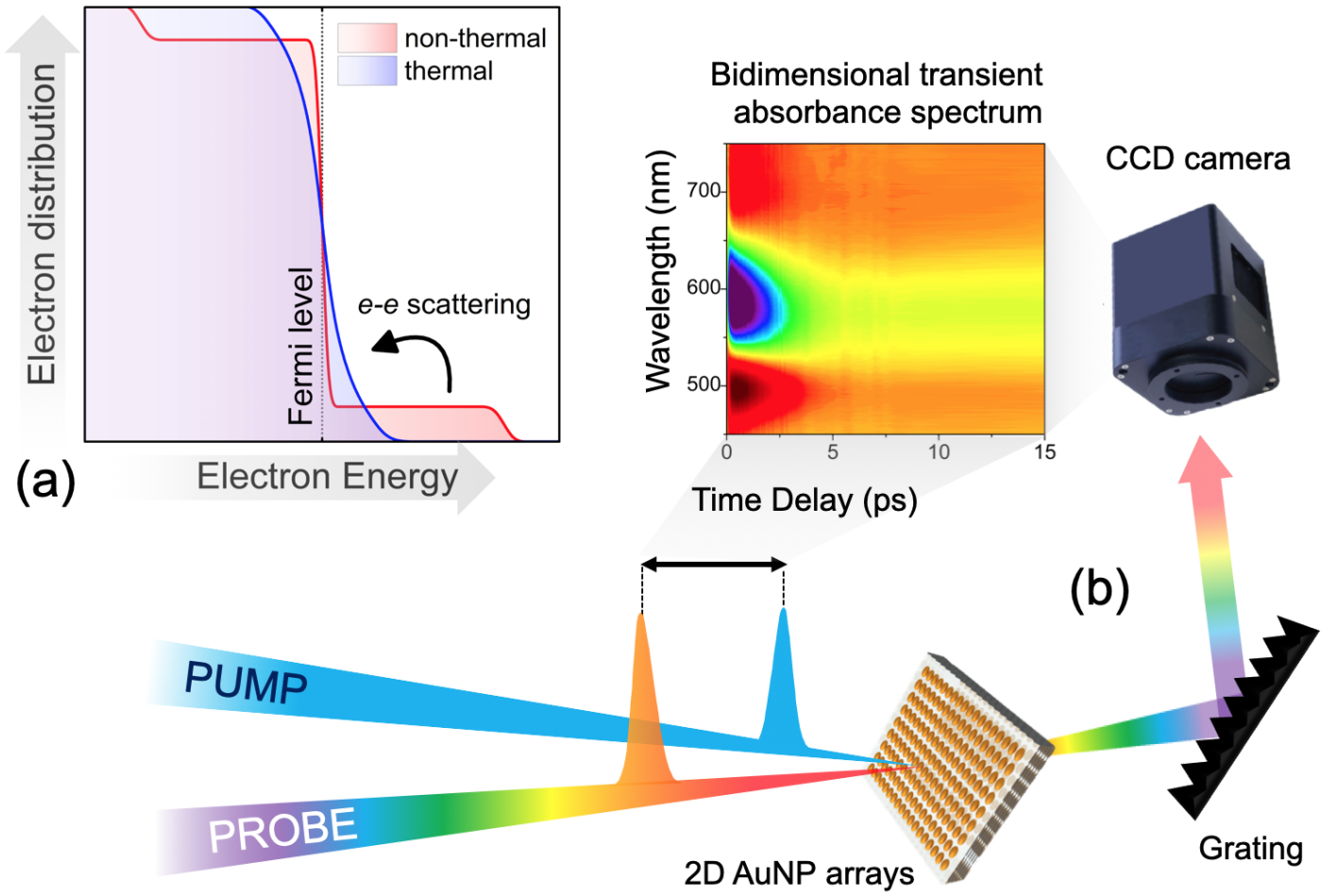

Figure 1: (a) Schematic representation of the nascent nonthermal electron distribution and of the subsequent thermal distribution produced by the electron thermalization process. The actual shape of the nascent distribution is hotly contested in the literature and depends strongly on the metal, nanostructure shape and type of excitation (see text for details). Here the intention is only to graphically illustrate how the nascent nonthermal distribution differs significantly from a thermal Fermi-Dirac distribution. (b) Schematic outline of the all optical pump-probe set-up (transmission mode) used to characterize the hot electron generation in gold nanostructures. The schematic geometry of the 2D gold nanoparticle arrays is also showed.

The excited electrons quickly collide and exchange their energies with many lower-energy electrons (electron thermalization) producing a thermalized electron distribution characterized by an overall increased electron temperature [19, 20, 21].

As extensively discussed in literature, an accurate description of the optical phenomena occurring in plasmonic nanostructures requires the electron excitation to be dealt with from different perspectives [22, 23, 24, 25], such as the quasi-classical description [26] (including the Drude model and the kinetic Boltzmann approach) and the quantum formalism. [27] In particular, quantum effects have to be accounted for when describing the generation of high-energy nonthermal electrons. [2, 28, 29]

Figure 1a reports a schematic representation of the nascent nonthermal electron distribution and of the subsequent thermal distribution produced after electron-electron scattering takes place. This is a simplified illustration, as the true energy distribution of the excited electrons depends on a number of factors, including the electronic band structure, [30, 31, 29, 32] dimensionality and geometric characteristics [33, 25, 34] of the metal nanostructure, the type [35, 29] and the intensity [36] of the excitation. In particular, nanostructures can display regions of electromagnetic energy accumulation, i.e. hot spots. The role of hot spots in the efficient production of nonthermal high-energy electrons has largely been highlighted. [17, 37, 38]

The lifetime of the initially out-of-equilibrium electron distribution depends on the collision dynamics

within the electronic population and can extend up to hundreds of femtoseconds. [36, 39, 40] After, and partially during, the initial electron thermalization, electrons lose further energy by externally thermalizing with the lattice through electron-phonon collisions. This leads to a thermal equilibrium of the entire nanostructure in several picoseconds. On a longer time scale (up to hundreds of picoseconds, even nanoseconds depending on the size of the nanostructure), the energy within the plasmonic structure dissipates to the environment through phonon-phonon scattering. [39]
The successful development of technologies which exploit hot electrons generated by plasmonic nanostructures, requires a deep understanding of both the energy distribution of the excited electrons and their fate/dynamics. The lifetime for the thermalization of photoexcited electron distributions in gold has been evaluated using a wide range of techniques (e.g. time-resolved photoelectron spectroscopy, [41] second harmonic generation, [42] transient absorbance [43, 44, 19, 33] and reflectivity, [45] four wave mixing [46, 47]) on a wide range of targets (e.g. thin films, [48] nanoparticles, [33] nanostructures [49]) and is generally evaluated to be between 200 and 500 fs although in some cases even shorter lifetimes [47, 50] have been observed. In this context, the observation of spectroscopic phenomena [51, 52] on short timescales (less than one hundred femtoseconds), has been attributed to the relevant contribution from highly energetic non thermalized electrons: their relaxation is expected to be very rapid due to the higher scattering rate of higher energy electrons. [43, 53] The enhancement of these ultrafast behaviours in metastructures and nanocrystals with complex shapes, has been correlated with the larger efficiency of these structures in the generation of highly energetic nonthermal electrons, due to hot spots and surface effects. [28, 50]
Here, we propose a combined experimental and theoretical approach to identify the specific dynamics of the nonthermal electrons generated upon photoexcitation of a plasmonic nanostructure. In particular, an array of gold nanoparticles deposited on a LiF substrate will be investigated through femtosecond transient absorbance spectroscopy (FTAS). The contributions of the nonthermal and thermal electron distributions to the optical response of this sample will be disentangled and relevant information on their dynamics will be inferred by the temporal evolution of the plasmon bleaching tail in the transient absorbance (TA) spectrum. In order to account for the strong out-of-equilibrium character of the initial electron distribution, the Extended two Temperature Model (E2TM) [48] will be used for the simulations. E2TM is an extension of the traditional Two Temperature model (TTM), [54] and provides a more accurate description of the fast relaxation dynamics of a photoexcited nanostructure, as it considers not only the electron bath and lattice temperatures, but also the initial nonthermal electron distribution. We will show how this theoretical approach allows us to reproduce the peculiar relaxation dynamics experimentally observed at different probe wavelengths, suggesting a subtle correlation between the spectral range experimentally probed and the energy of the occupied electronic states.

2 Results and discussion

The static transmission spectrum of 2D arrays of Au nanoparticles (NPs), measured with light linearly polarized along the main axis of the NPs, shows a pronounced dip at 595 nm ascribable to the longitudinal surface plasmon resonance (SPR) of the nanoellipsoids, superimposed on a broad band due to interband transitions from 5d to 6sp states of gold (Figure S1 of the Supporting Information).
Figure 2a shows the false-colour TA map of the sample, when excited by a 405 nm pump beam at 20 μJ cm^{-2}, which corresponds mainly to interband excitation with a small plasmonic contribution (see Figure S1). A negative signal around 600 nm, with two positive wings on both sides, can be observed. These features can be attributed to the bleaching of the longitudinal SPR, which is due to the alterations of the optical properties of the NPs upon excitation by the femtosecond pump beam: nonthermal electrons are generated, then thermalize with the other electrons through electron-electron scattering and relax.[39] As known, heating causes depletion and broadening of the plasmon resonance. As a result a bleaching of the probe signal quickly appears together with two positive wings on either side of the bleaching in the TA spectrum.[55] These features decay in the first few picoseconds due to electron-phonon coupling, then the nanoparticle returns to its unperturbed state in tens/hundreds of picoseconds.

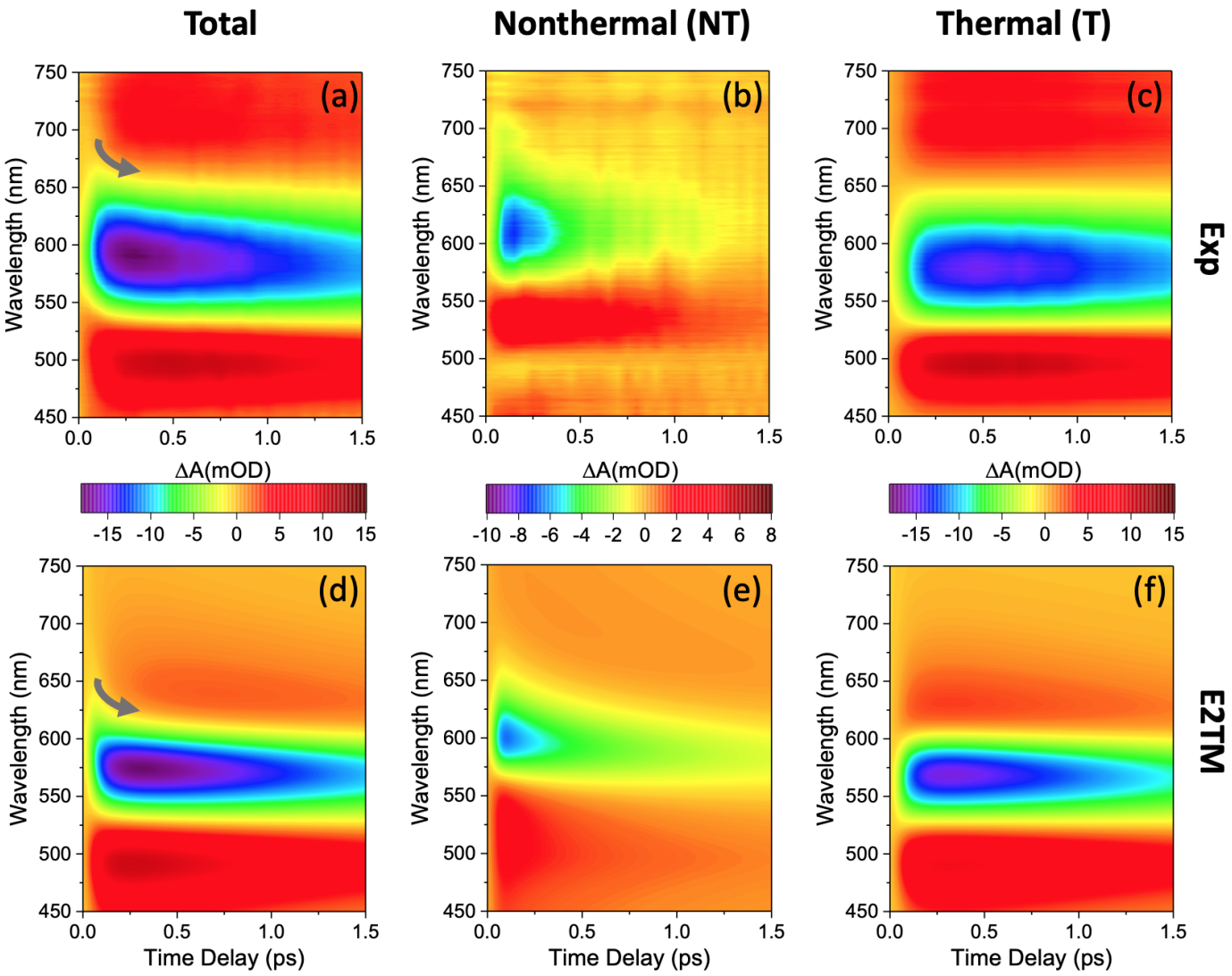

Figure 2: (a) Experimental false-colour TA map of the 2D arrays of Au NPs following photoexcitation at 405 nm light pulse with 20 μJ cm^{-2}. The electric field polarization of the pump and probe beams are parallel to the major axis of the NPs. False-colour TA maps for (b) NT and (c) T electron distributions, obtained with the procedure described in the text. (d-f) Predicted false-colour TA maps of isolated nanoellipsoids excited with 20 μJ cm^{-2} of radiation at 400 nm and separate contributions from NT and T electron distributions, respectively. The simulations have been conducted with E2TM. An arrow in (a) and (d) highlights the rapid change in the transient spectra.

A fast modification of the TA spectrum is observed in the long-wavelength tail of the plasmonic feature (see the dark arrow in the wavelength region over 650 nm in Figure 2a), that shows a shifting of the band towards the blue, in the first hundreds of femtoseconds. Such fast dynamics on the tail of the plasmonic resonance has already been observed in the literature (see, e.g., Refs. [56, 48]) but not investigated in detail.

To shed light on this behavior, we have simulated the transient optical response of our system and the specific contributions coming from both nonthermal (NT) and thermal (T) electrons, and lattice. Figure 2d shows the simulated TA map for 20 μJ cm^{-2} pump fluence at 400 nm wavelength. As can be seen, theoretical calculations reproduce the experimental data very well, including, in particular, the ultrafast feature observed on the short timescale in the long wavelengths range. We observe a larger spectral width of the bleaching band in the experimental map, possibly due to a size distribution of the nanoellipsoids in the real sample. This polydispersity is not fully taken into account in the simulations (see the *Theoretical Details* in the Methods section).

The transient optical response of the Au NPs array reflects the temporal evolution of its dielectric function, which in turn can be related to the time dependent changes of the electron distribution.[19, 43] Breaking down the predicted TA map of Figure 2d into the transient optical responses due to NT and T electrons and lattice (not shown here because of the picosecond time scale under consideration) allows us to disentangle their separate contributions to the relaxation of the photoexcited nanostructure. Figure 2e-f report the simulated TA maps of the NT and T electron energy distribution using the E2TM model. As can be seen, the NT electrons show a very fast evolution in the first few hundreds of femtoseconds, contrary to the dynamics of T electrons which is much more limited on this time scale. Indeed, the overall optical response (labelled Total in Figure 2a and d) is dominated by T electrons on a time delay longer than 1 picosecond, i.e. after the disappearance of the contribution from NT electrons which only contribute to the signal in the first few hundreds of femtoseconds. Furthermore, the NT electrons TA spectra are red shifted compared to those belonging to T electrons (and lattice), with NT electrons mainly contributing to the short timescale optical response in the long-wavelength tail of the plasmon bleaching. Thus, the rapid change of the signal in this spectral region, highlighted by dark arrows in the maps of Figure 2a and d, appears to be due to the interplay between the contributions of NT and T electrons.

The observation that NT and T contributions play a role in different temporal and spectral ranges suggests the possibility of isolating these contributions also in the Total experimental TA map. Looking at the simulated TA maps of Figure 2e-f, we have selected a wavelength where the intensity of the thermal contribution is dominant with respect to the nonthermal contribution, i.e. 500 nm, and a time delay when the dynamics of the NT electrons has almost expired, i.e. 2 ps. We have extracted the temporal cut at 500 nm (intensity profile of the TA signal at 500 nm as a function of the time delay) and the TA spectrum at 2 ps from the Total experimental map of Figure 2a. Then we have used the temporal cut to modulate the TA spectrum (see Figure S2 for more details) obtaining a map, i.e. the TA spectrum acquired at 2 ps was used as a spectral template whose time-dependent intensity was given by the profile of the temporal cut at 500 nm.

The resulting map, with a dominant contribution from T electrons, is reported in Figure 2c as the Thermal map. In principle, by subtracting this Thermal map from the Total experimental TA map, one can obtain a TA map originating from NT electrons only. Figure 2b reports the NT map obtained by using such a procedure, i.e. making the point-by-point difference between the experimental TA maps of Figure 2a and 2c. A very good agreement can be observed with the simulations (compare Figure 2b with Figure 2e).

This procedure has been repeated using different temporal cuts in the range 530±30 nm, with no significant change of the final result, thus demonstrating the robustness of the method.

The quality of this combined experimental and simulation approach is even more evident if we examine the temporal cuts obtained from the TA maps of Figure 2. **Figure 3** reports a comparison of the experimental and simulated dynamics of the Total signal and of the NT and T contributions. As the widths of the plasmon bleaching signals in the experimental and simulated TA spectra are slightly different, we

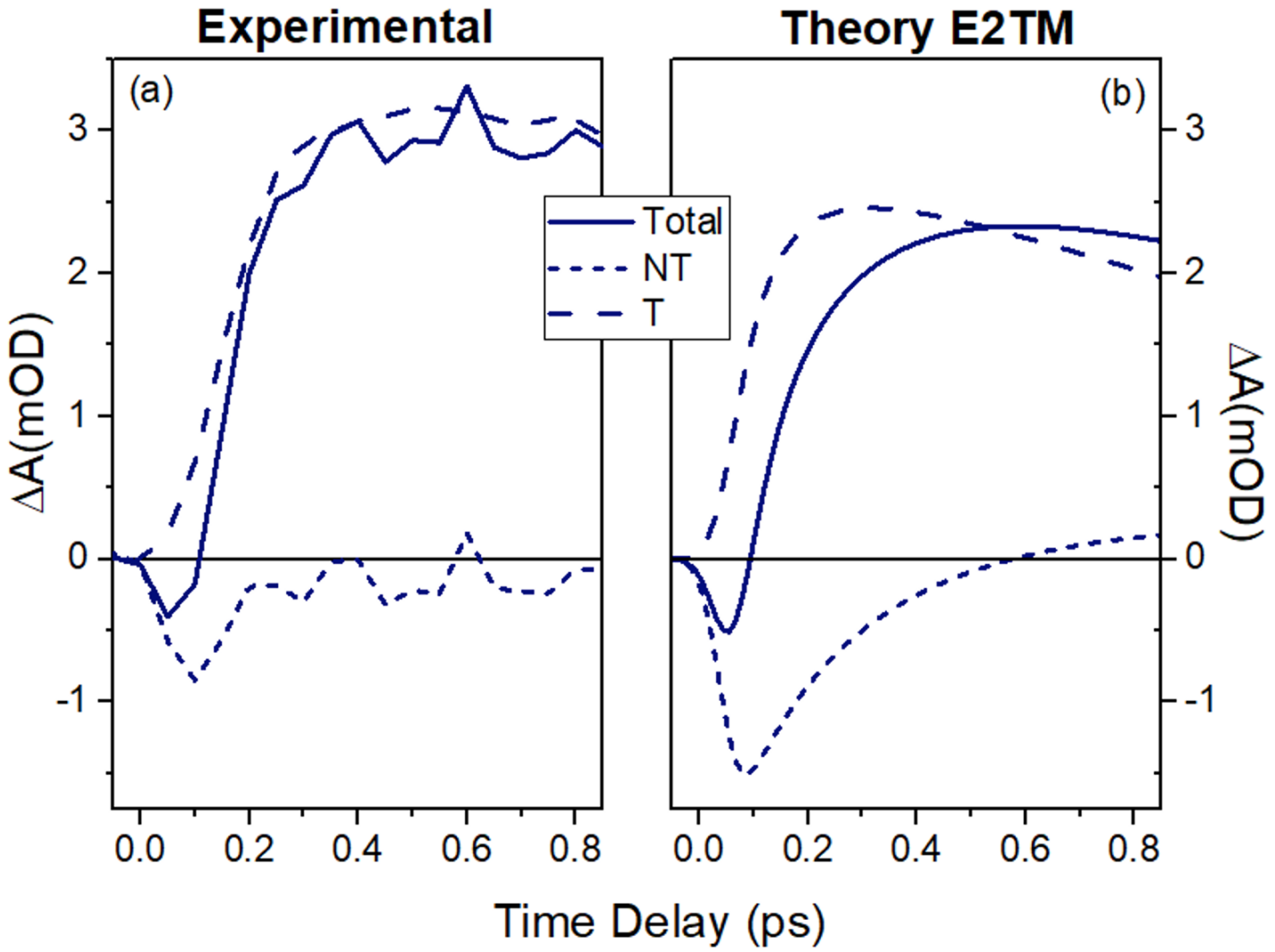

Figure 3: Total, NT and T temporal cuts obtained from the (a) experimental and (b) E2TM simulated TA maps of Figure 2a-f. As discussed in the text, we have considered cuts at 680 nm for the experimental TA spectra and at 650 nm for the simulated TA spectra.

have considered cuts at 680 nm and 650 nm, respectively.

The E2TM reproduces very well the transient shape of the nonthermal signal, which clearly affects only the first hundreds of femtoseconds of the total temporal cut. As expected, the rise time of the NT profile appears to be comparable to the instrument response function (IRF), as the NT electrons are produced on the timescale of the pump pulse duration, while the delayed rise time of the T profile reflects the build up of the thermalized electron distribution due to electron-electron (and partially electron-phonon) scattering.[43, 57] The E2TM simulations also succeeded in reproducing (at least qualitatively) the peculiar changes in the relaxation dynamics when observed at different probe wavelengths. **Figure 4**a reports some temporal cuts of the nonthermal contribution to the TA signal, extracted from the experimental map of Figure 2b at different probe wavelengths (from 600 nm to 675 nm) along the feature of the plasmon bleaching. These cuts clearly highlight a remarkable feature of the TA signal: a faster decay is observed when moving from shorter to longer probe wavelengths. A comparison with simulations can help us to understand this behaviour.

Figure 4b shows temporal cuts of the maps of Figure 2e, representing the simulated contribution to TA spectra arising from NT electrons according to the E2TM. For comparison, we also show, in Figure 4c, the theoretical prediction retrieved by the more basic Three Temperature Model (3TM) (see, e.g., Refs. [43, 51]). As clearly visible, the 3TM is unable to reproduce the observed temporal profiles of Figure 4a which are well simulated by the E2TM. Both models take into account the out-of-equilibrium character of the

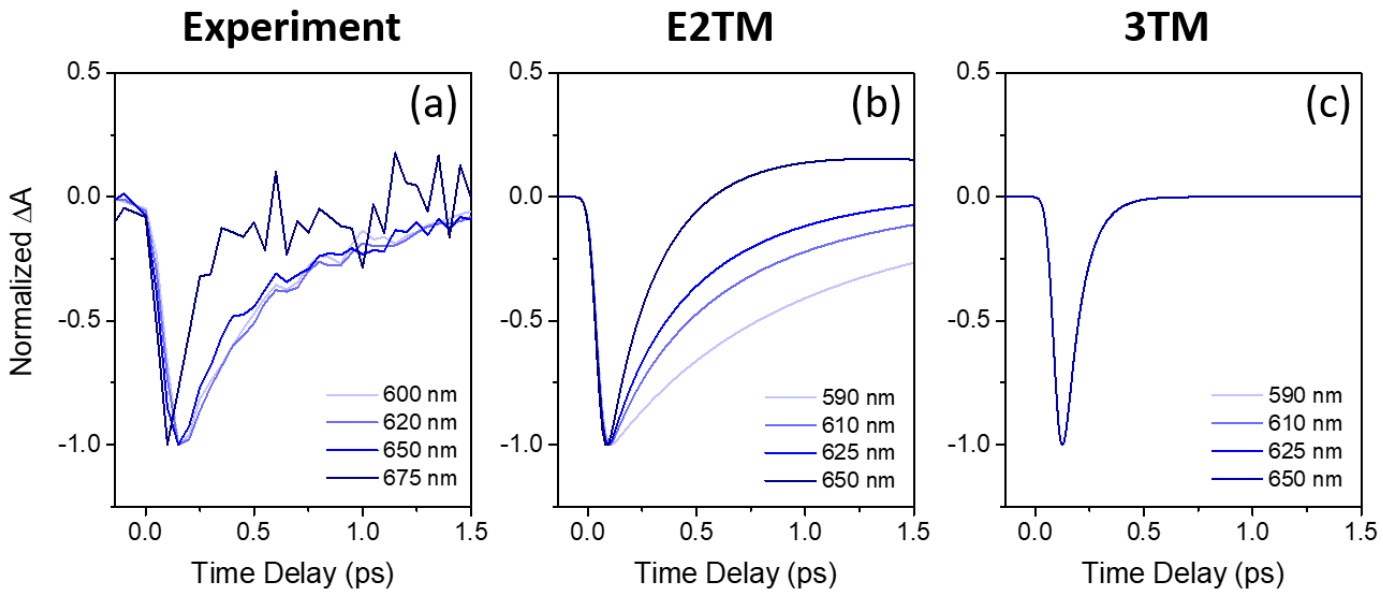

Figure 4: Temporal cuts at different probe wavelengths of the NT contribution extracted from (a) the experimental TA map and from the simulated TA maps obtained by (b) E2TM and (c) 3TM models. The 3TM TA map is reported in Figure S3 of the Supporting Information.

nascent electron distribution, but provide a different description in terms of decay dynamics: the 3TM considers a single NT population which relaxes with a single electron-electron scattering rate for all the electron energies involved, while in the E2TM this rate depends upon the energy of the scattering electrons. [51] Accordingly, as the NT electrons have a broad energy distribution below and above the Fermi level, the E2TM predicts different relaxation dynamics for electrons with different energies (see *Theoretical Details* in the Methods section).

However, note that, a priori, there should be no correspondence between the energy of NT electrons and the energy (or wavelength) of probe photons, and a more refined analysis ought to be given in order to explain the origin of the observed correlation. This can be done by resorting to the E2TM, and in particular by inspecting the semiclassical calculations employed to retrieve the modulation of gold permittivity (which is the optical parameter that governs any TA measurements) starting from the pump-induced modulation of NT electrons occupation probability, $\Delta_{NT}(E,t)$. This calculation is detailed in Equation (3) of the Methods section, and shows that when looking at the optical effects caused by changes in the electrons distribution we have also to consider the precise structure of the available states in the valence and conduction band for the given photon wavelength, which is formally taken into account by the ED-JDOS function $D(E,\lambda)$ (cf. *Theoretical Details* in the Methods section). It is thus not just $\Delta_{NT}(E,t)$ that one should consider when interpreting the TA spectra, rather the product function $S_{NT}(E,\lambda,t) = D(E,\lambda)\Delta_{NT}(E,t)$.

Figure 5 shows a cross-section map of S_{NT} computed at $t = \bar{t} = 100$ fs time delay. The horizontal axis is the electron energy in the conduction band measured from the Fermi level, and the vertical axis is the probe wavelength. The map clearly shows how, for a given probe wavelength, the range of electron energies contributing to the optical response dramatically changes. The top panel inset is a projection of $S_{NT}(E,\lambda,\bar{t})$ on the (E,S_{NT}) plane, and indicates that in the considered wavelength range the dynamics is dominated by low energy NT electrons. A more refined argument is given by estimating the average electrons energy $\langle E \rangle$ involved in optical transitions at a given probe wavelength λ, using $|S_{NT}(E,\lambda,\bar{t})|$ as the weighting function. The result is shown in the right panel inset of Figure 5 and points in favor of a negative dispersion of the λ versus $\langle E \rangle$ function, i.e., when moving from shorter to longer wavelengths of the probe, the range of electron energies involved in the transient optical response moves from higher to lower mean values. This is consistent with the general picture according to which the transient permittivity modulation from photogenerated hot electrons in gold is governed by Pauli blocking of direct in-

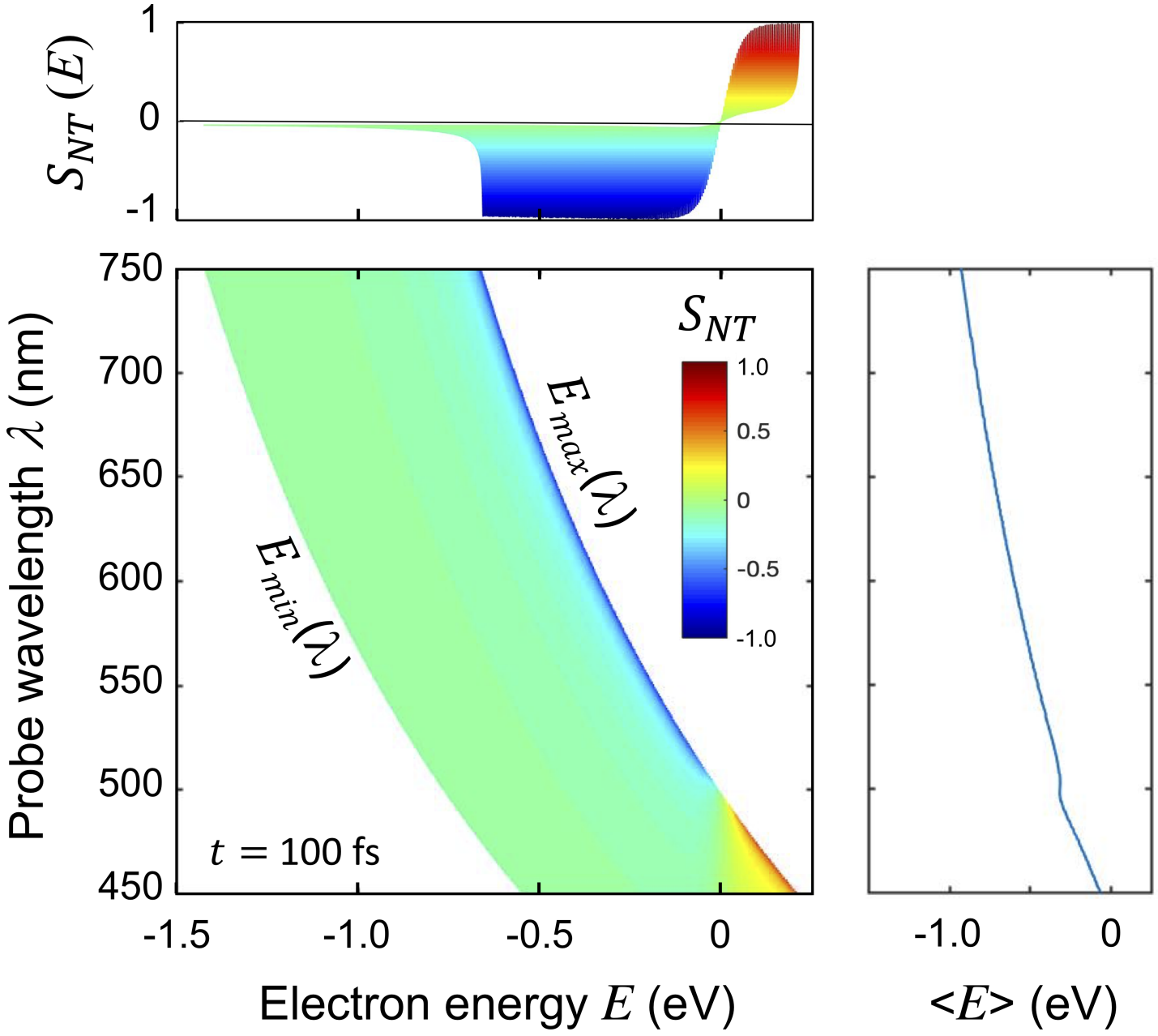

Figure 5: Map of S_{NT} at 100 fs pump-probe delay, as a function of conduction band electron energy (measured from the Fermi level), and wavelength λ of the considered optical transition (see *Theoretical Details* in the Methods section). The top inset shows, for a 100 fs pump-probe delay, the projection of $S_{NT}(E,\lambda)$ on the (E,S_{NT}) plane. The right inset shows the average energy of the electrons that are contributing to the modulation of the interband transition as a function of the optical wavelength at 100 fs pump-probe delay.

terband transitions. In this way, it is clear that longer probe wavelengths in the visible spectrum involve unoccupied electron states below the Fermi level. Furthermore, the more energetically distant these states are from the Fermi level the longer is the photon wavelength. If we now remember that the electron-electron scattering rate increases for electrons with increasing energy distance from the Fermi level, i.e. $1/\tau_{ee}(E)$ $(E/E_F)^2$ (see *Theoretical Details* in the Methods section), it is clear that the decay of the transient optical signal observed at longer wavelengths ought to be faster than that observed at shorter wavelengths, in agreement with the experimental results of Figure 4a.

3 Conclusion

The photoexcitation of plasmonic nanostructures is well known to give rise to two populations of electrons, with very different energy distributions: nonthermal electrons, characterized by a broad distribution of energies, and thermal electrons (described in terms of a Fermi-Dirac distribution at a higher temperature) having an energy spectrum peaked around the Fermi level. The coupling between the two is extremely fast, being established by electron-electron scattering, taking place in a few hundred femtoseconds. The study of nonthermal electron dynamics is thus typically accomplished by indirect methods, based on Boltzmann transport equation numerical simulations. Here we demonstrate how femtosecond transient absorption spectroscopy guided by nonlinear optics modeling based on the agile E2TM gives a more direct access to nonthermal electron dynamics in plasmonic nanostructures. In particular, our approach has been applied to an array of gold nanoparticles deposited on a LiF substrate. The theoretical prediction from the E2TM, according to which the transient optical response observed at different photon energies correlates with selected energies within the broad spectrum of the photogenerated nonthermal electrons, is confirmed by our measurements. This result provides a clearcut evidence that the relaxation dynamics observed in the visible and near infrared turned out to be dominated by the low energy tail of the nonthermal electrons. The capability to spectrally separate the contributions from nonthermal and thermal electrons in TA measurements provides a noninvasive semiempirical tool to determine the energy content and lifetime of highly energetic electrons in plasmonic nanostructures. Such a characterization is of key relevance for the optimization of hot electrons enhanced processes in a variety of contexts, from light harvesting to photocatalysis and nonlinear nanophotonics.

4 Methods

Experimental details:
The FTAS measurements in the pump and probe scheme were performed with a laser system consisting of a chirped pulse amplifier seeded by a Ti:Sa oscillator. The pump pulses were produced by frequency doubling of the 810 nm fundamental (405 nm). The white light probe (350 - 800 nm), on the other hand, was generated in a commercial TA spectrometer (FemtoFrame II, IB Photonics) employing a split beam configuration in which 50% of the white light passes through (transmission mode) or is reflected by (reflection mode) the sample, while the remainder is used as a reference to account for pulse-to-pulse fluctuations in the white light generation. The pump pulse is loosely focused (circular spot of diameter = 500 μm) onto the sample with an energy density of 20 μJ cm^{-1}, which is at least an order of magnitude below the melting threshold of the particles. [58, 59] The spot diameter of the probe pulse is much smaller (approx. 150 μm, 10 μJ cm^{-1}) and its time delay with respect to the pump pulse is scanned in time by varying the length of its optical path. The IRF was measured to be 50 fs (Gaussian FWHM) by the fastest rise time detectable in the TA spectra. All measurements were performed in air at room temperature. Figure 1b reports a schematic outline of the pump-probe set-up in the transmission mode. Unless otherwise noted, the measurements reported in this work have been performed with this configuration. Further details of the pump-probe set-up can be found in previous publications. [60, 61, 62]
The sample consisted of 2D arrays of AuNPs deposited onto the surface of a nanopatterned LiF(110) single crystal (see Figure 1b). [63] The NPs were fabricated by depositing 4 nm of Au onto the self-organized

nanometric uniaxial ridge-valley pattern that develops upon high-temperature homoepitaxial growth onto LiF(110) substrates (Crystech Gmbh).[64] Au (Mateck GmbH, 99.99% purity) was deposited at room temperature in high vacuum by molecular beam epitaxy at 60° of incidence with respect to the surface normal. The sample was subsequently annealed at T=670 K in order to induce the thermal dewetting of the deposited metal and the formation of an array of NPs, arranged in closely-spaced linear chains, coherently oriented all over the sample. The array pitch along (transverse to) the chains was 39±5 nm (26±4 nm). The NPs, schematized as prolate ellipsoids lying along the substrate ripples had mean semiaxes of 13±4 nm and 9±3 nm, along and transverse to the ripples, respectively. The electric field polarization of the pump and probe beams have been set parallel to the major axis of the ellipsoidal NPs, allowing us to selectively probe the longitudinal surface plasmon resonances of the NPs (see the static transmission spectrum in Figure S1 of the Supporting Information).

Theoretical details:

In view of the self-assembling process that governs the formation of the nanopaticles array, we modeled the sample as a collection of non-interacting prolate nanoellipsoids with semiaxes $a = 16$ nm, $b = c = 7$ nm and particle concentration detailed by the array pitch area S, corresponding to $\sim 10^3 \mu\text{m}^{-2}$. We adopted the effective environment approximation, widely employed in nanooptics (see, e.g., Refs. [65, 66]), according to which the supported nanoobject is embedded in a homogeneous environment with an effective permittivity $\epsilon_e = (n_1^2 + n_2^2)/2 = 1.466$, where $n_1 = 1.39$ and $n_2 = 1$ are the refractive indexes of the substrate (LiF) and of the cover (air), respectively. Plasmon hybridization and disorder along the array, as well as surface roughness effects in the nanostructures compared to bulk gold, are well known to result into a broadening of the optical spectra compared to the ideal spectrum of the individual nanoellipsoids. By following the approach reported by Wegener and coworkers [67], this broadening was mimicked by increasing the Drude damping parameter Γ of Au permittivity with respect to its bulk value $\Gamma_0 \simeq 70$ meV (we found a factor $\Gamma/\Gamma_0 \simeq 6$ quite satisfactory). These assumptions enabled an accurate quantitative modeling of the optical response of the sample by using quasi-static formulas, starting from the nanoellipsoid polarizability tensor with in-plane components $\alpha_{x,y} = V\epsilon_0(\epsilon_m - \epsilon_e)/[L_{x,y}\epsilon_m + (1 - L_{x,y})\epsilon_e]$ and out-of-plane component $\alpha_z = \alpha_y$ (see e.g. Ref. [68]). In previous formulas, x is the direction of the major axis of the nanoellipsoid, ϵ_0 is the vacuum permittivity, V is the volume and ϵ_m the permittivity of the nanoellipsoid, and L_x, L_y are the so-called *depolarization factors*. For ϵ_m we assumed gold dielectric function given by a Drude-Lorentz model [69], fitted on Johnson and Christy experimental data.[70] The absorbance is finally modeled as $A = -\log_{10}(T)$, with $T = \exp(-\sigma_E/S)$ the sample transmittance, and σ_E the total extinction cross-section of the individual nanoellipsoid, retrieved (according to quasi-static formulas [68]) from polarizability component α_x, being the sample illuminated with x-polarized light.

Regarding transient optical simulations, we modelled the pump-induced optical modulation of gold permittivity as a function of the probe wavelength λ and the pump-probe time delay t by following the same approach already reported by one of the present authors in previous studies,[48, 49] based on a refined version of the two-temperature model,[71] also referred to as E2TM. [48] In short, this model is capable of capturing the ultrafast (sub picosecond) temporal dynamics of NT carriers photogenerated in gold after excitation with fs-laser pulses as well as the subsequent electron-electron and electron-phonon thermalization. This is accomplished by assuming that an intense optical (pump) pulse of photon energy $h\nu_P$ is capable of promoting a free carrier from below to above the Fermi energy E_F, giving rise to a temporal modulation of the electron occupation probability according to the following expression:

$$\Delta f_{NT}(E,t) = 1/A \times \Delta_{NT}(E) \int_{-\infty}^{t} P_a(t') e^{-(t-t')/\tau(E)} dt', \tag{1}$$

with

$$\tau(E) = \frac{\tau_{ep}\tau_{ee}(E)}{\tau_{ep} + \tau_{ee}(E)}. \tag{2}$$

In the above equations, P_a is the pump power density absorbed in the Au structure, A is a normalization constant determined from energy conservation law, τ_{ep} is the electron-phonon scattering time constant, E is the electron energy measured from the Fermi energy, $\tau_{ee}(E) \propto (E_F/E)^2$ is the electron-electron

scattering time, and $\Delta_{NT}(E)$ is a double-steplike function, extending from $-h\nu_P$ to $+h\nu_P$ (see Ref. [48] and references therein for further details).
The E2TM also provides the temporal evolution of the electronic temperature $\Theta_e(t)$ which is then employed to compute the corresponding modulation of thermal electrons occupation probability $\Delta f_T(E,t)$, according to the Fermi smearing mechanism.[48]
The variation of electrons occupation probability for nonthermal (thermal) electrons, $\Delta f_{NT(T)}(E,t)$, gives rise to a modulation of the absorption probability for d-band to conduction band transitions near the L point in the irreducible zone of the Brillouin cell, which is accounted for in terms of a variation of the so-called *Joint Density of States* (JDOS) [72]:

$$\Delta JDOS(\lambda,t) = -\int_{E'(\lambda)}^{E''(\lambda)} D(E,\lambda)\Delta f_{NT(T)}(E,t)dE, \tag{3}$$

where $D(E,\lambda)$ is the *Energy Distribution of the Joint Density of States* (EDJDOS) of the considered optical transition, numerically computed under the parabolic band approximation [72]. The effective masses, energy gaps, dipole matrix element and integration limits E' and E'' are taken from Ref. [73].
The variation of the imaginary part of gold permittivity $\Delta\epsilon''(\lambda,t)$ is then straightforwardly computed under the constant matrix element approximation, being linearly proportional to $\lambda^2\Delta JDOS(\lambda,t)$, and the corresponding real part variation $\Delta\epsilon'(\lambda,t)$ is obtained by Kramers-Kronig transformation of $\Delta\epsilon''(\lambda,t)$. [74, 72]
As per the lattice heating effects, we have followed the same approach detailed in Ref. [49], assuming a linear increase of the Drude damping and a linear decrease of the plasma frequency as a function of the lattice temperature, thus resulting in a modulation of the Drude permittivity contribution to the gold dielectric function.
The transient absorbance was finally computed in the quasi-static limit by replacing the steady state Au permittivity $\epsilon_m(\lambda)$ with the dynamic permittivity $\epsilon_m(\lambda)+\Delta\epsilon(\lambda,t)$ in the nanoellipsoid polarizability and extinction cross-section formulas, $\Delta\epsilon(\lambda,t)$ being the sum of all three contributions to Au permittivity modulation arising from NT electrons, T electrons and lattice.

Supporting Information
Supporting Information is available from the Wiley Online Library or from the author.

Acknowledgements
The authors thank F. Martelli for the fruitful discussions.

References

[1] M. L. Brongersma, N. J. Halas, P. Nordlander, *Nat. Nanotechnol.* **2015**, *10*, 1 25.

[2] A. O. Govorov, H. Zhang, H. V. Demir, Y. K. Gunko, *Nano Today* **2014**, *9*, 1 85 .

[3] N. Prineha, S. Ravishankar, A. H. A., *Nanophotonics* **2016**, *5* 96.

[4] T. G. Deepak, X. Zhenhe, L. Yanlong, I. Ricardo, M. Dongling, *Nanophotonics* **2017**, *6* 153.

[5] L. Zhou, D. F. Swearer, C. Zhang, H. Robatjazi, H. Zhao, L. Henderson, L. Dong, P. Christopher, E. A. Carter, P. Nordlander, N. J. Halas, *Science* **2018**, *362*, 6410 69.

[6] H. Tang, C.-J. Chen, Z. Huang, J. Bright, G. Meng, R.-S. Liu, N. Wu, *The Journal of Chemical Physics* **2020**, *152*, 22 220901.

[7] A. Schirato, M. Maiuri, A. Toma, S. Fugattini, R. P. Zaccaria, P. Laporta, P. Nordlander, G. Cerullo, A. Alabastri, G. D. Valle, *Nature Photonics* **2020**, *14*, 12 723.

[8] Y. Zhang, S. He, W. Guo, Y. Hu, J. Huang, J. R. Mulcahy, W. D. Wei, *Chem. Rev.* **2018**, *118*, 6 2927.

[9] E. Cortés, W. Xie, J. Cambiasso, A. S. Jermyn, R. Sundararaman, P. Narang, S. Schlücker, S. A. Maier, *Nat. Commun.* **2017**, *8* 14880.

[10] C. Zhan, M. Moskovits, Z.-Q. Tian, *Matter* **2020**, *3*, 1 42.

[11] S. Linic, P. Christopher, D. B. Ingram, *Nat. Mater.* **2011**, *10* 911.

[12] M. L. Brongersma, *Proc. IEEE* **2016**, *104*, 12 2349.

[13] C. Clavero, *Nat. Photonics* **2014**, *8* 95.

[14] L. Wei, V. J. G., *Nanophotonics* **2017**, *6* 177.

[15] S. M. A. Mirzaee, O. Lebel, J.-M. Nunzi, *ACS Appl. Mater. Interfaces* **2018**, *10*, 14 11862.

[16] N. Wu, *Nanoscale* **2018**, *10* 2679.

[17] G. V. Hartland, L. V. Besteiro, P. Johns, A. O. Govorov, *ACS Energy Lett.* **2017**, *2*, 7 1641.

[18] S. Link, M. A. El-Sayed, *Int. Rev. Phys. Chem.* **2000**, *19*, 3 409.

[19] C. Voisin, N. Del Fatti, D. Christofilos, F. Vallée, *J. Phys. Chem. B* **2001**, *105*, 12 2264.

[20] S. Link, C. Burda, Z. L. Wang, A. El-Sayed, *J. Chem. Phys.* **1999**, *111*, 3 1255.

[21] J. G. Liu, H. Zhang, S. Link, P. Nordlander, *ACS Photonics* **2018**, *5*, 7 2584.

[22] J. Aizpurua, F. Baletto, J. Baumberg, P. Christopher, B. de Nijs, P. Deshpande, Y. D. Fernandez, L. Fabris, S. Freakley, S. Gawinkowski, A. Govorov, N. Halas, R. Hernandez, B. Jankiewicz, J. Khurgin, M. Kuisma, P. V. Kumar, J. Lischner, J. Liu, A. Marini, R. J. Maurer, N. S. Mueller, M. Parente, J. Y. Park, S. Reich, Y. Sivan, G. Tagliabue, L. Torrente-Murciano, M. Thangamuthu, X. Xiao, A. Zayats, *Faraday Discussions* **2019**, *214* 245.

[23] L. Chang, L. V. Besteiro, J. Sun, E. Y. Santiago, S. K. Gray, Z. Wang, A. O. Govorov, *ACS Energy Letters* **2019**, *4*, 10 2552.

[24] L. V. Besteiro, P. Yu, Z. Wang, A. W. Holleitner, G. V. Hartland, G. P. Wiederrecht, A. O. Govorov, *Nano Today* **2019**, *27* 120.

[25] L. V. Besteiro, X.-T. Kong, Z. Wang, G. Hartland, A. O. Govorov, *ACS Photonics* **2017**, *4*, 11 2759.

[26] D. B. Tanner, *Optical Effects in Solids*, Cambridge University Press, **2019**.

[27] U. Kreibig, M. Vollmer, *Optical Properties of Metal Clusters*, volume 25, Springer Berlin Heidelberg, **1995**.

[28] M. E. Sykes, J. W. Stewart, G. M. Akselrod, X.-T. Kong, Z. Wang, D. J. Gosztola, A. B. F. Martinson, D. Rosenmann, M. H. Mikkelsen, A. O. Govorov, G. P. Wiederrecht, *Nature Communications* **2017**, *8*, 1 986.

[29] A. M. Brown, R. Sundararaman, P. Narang, W. A. Goddard, H. A. Atwater, *ACS Nano* **2016**, *10*, 1 957.

[30] R. Sundararaman, P. Narang, A. S. Jermyn, W. A. Goddard III, H. A. Atwater, *Nat. Commun.* **2014**, *5* 5788.

[31] F. Ladstädter, U. Hohenester, P. Puschnig, C. Ambrosch-Draxl, *Phys. Rev. B* **2004**, *70*, 23.

[32] T. P. Rossi, P. Erhart, M. Kuisma, *ACS Nano* **2020**, *14*, 8 9963.

[33] C. Voisin, D. Christofilos, P. A. Loukakos, N. D. Fatti, F. Vallée, J. Lermé, M. Gaudry, E. Cottancin, M. Pellarin, M. Broyer, *Phys. Rev. B* **2004**, *69*, 19 195416.

[34] A. Manjavacas, J. G. Liu, V. Kulkarni, P. Nordlander, *ACS Nano* **2014**, *8*, 8 7630.

[35] J. Zhao, S. C. Nguyen, R. Ye, B. Ye, H. Weller, G. A. Somorjai, A. P. Alivisatos, F. D. Toste, *ACS Cent. Sci.* **2017**, *3*, 5 482.

[36] N. Del Fatti, C. Voisin, M. Achermann, S. Tzortzakis, D. Christofilos, F. Vallée, *Phys. Rev. B* **2000**, *61* 16956.

[37] L. V. Besteiro, A. O. Govorov, *J. Phys. Chem. C* **2016**, *120*, 34 19329.

[38] H. Zhang, A. O. Govorov, *J. Phys. Chem. C* **2014**, *118*, 14 7606.

[39] G. V. Hartland, *Chem. Rev.* **2011**, *111*, 6 3858.

[40] F. Bisio, E. Principi, M. Magnozzi, A. Simoncig, E. Giangrisostomi, R. Mincigrucci, L. Pasquali, C. Masciovecchio, F. Boscherini, M. Canepa, *Phys. Rev. B* **2017**, *96*, 8 081119.

[41] W. S. Fann, R. Storz, H. W. K. Tom, J. Bokor, *Phys. Rev. Lett.* **1992**, *68* 2834.

[42] C. Guo, G. Rodriguez, A. J. Taylor, *Phys. Rev. Lett.* **2001**, *86* 1638.

[43] C.-K. Sun, F. Vallée, L. H. Acioli, E. P. Ippen, J. G. Fujimoto, *Phys. Rev. B* **1994**, *50* 15337.

[44] S. Link, , M. A. El-Sayed, *J. Phys. Chem. B* **1999**, *103*, 40 8410.

[45] T. Heilpern, M. Manjare, A. O. Govorov, G. P. Wiederrecht, S. K. Gray, H. Harutyunyan, *Nat. Commun.* **2018**, *9*, 1 1853.

[46] S. Park, M. Pelton, M. Liu, P. Guyot-Sionnest, N. F. Scherer, *J. Phys. Chem. C* **2007**, *111*, 1 116.

[47] F. Masia, W. Langbein, P. Borri, *Phys. Rev. B* **2012**, *85* 235403.

[48] G. Della Valle, M. Conforti, S. Longhi, G. Cerullo, D. Brida, *Phys. Rev. B* **2012**, *86* 155139.

[49] G. Della Valle, D. Polli, P. Biagioni, C. Martella, M. C. Giordano, M. Finazzi, S. Longhi, L. Dué, G. Cerullo, F. Buatier de Mongeot, *Phys. Rev. B* **2015**, *91* 235440.

[50] H. Harutyunyan, A. B. F. Martinson, D. Rosenmann, L. K. Khorashad, L. V. Besteiro, A. O. Govorov, G. P. Wiederrecht, *Nat. Nano* **2015**, *10*, 9 770.

[51] M. Zavelani-Rossi, D. Polli, S. Kochtcheev, A.-L. Baudrion, J. Béal, V. Kumar, E. Molotokaite, M. Marangoni, S. Longhi, G. Cerullo, P.-M. Adam, G. Della Valle, *ACS Photonics* **2015**, *2*, 4 521.

[52] H. Baida, D. Mongin, D. Christofilos, G. Bachelier, A. Crut, P. Maioli, N. D. Fatti, F. Vallée, *Physical Review Letters* **2011**, *107*, 5.

[53] M. Bernardi, J. Mustafa, J. B. Neaton, S. G. Louie, *Nat. Commun.* **2015**, *6* 7044.

[54] S. I. Anisimov, B. L. Kapeliovich, T. L. Perel'Man, *Soviet Journal of Experimental and Theoretical Physics* **1974**, *39* 776.

[55] T. S. Ahmadi, S. L. Logunov, M. A. El-Sayed, *J. Phys. Chem.* **1996**, *100*, 20 8053.

[56] H. Inouye, K. Tanaka, I. Tanahashi, K. Hirao, *Phys. Rev. B* **1998**, *57*, 18 11334.

[57] A. M. Brown, R. Sundararaman, P. Narang, A. M. Schwartzberg, W. A. Goddard, H. A. Atwater, *Phys. Rev. Lett.* **2017**, *118* 087401.

[58] E. Boulais, R. Lachaine, M. Meunier, *J. Phys. Chem. C* **2013**, *117*, 18 9386.

[59] M. Magnozzi, R. P. Zaccaria, D. Catone, P. O'Keeffe, A. Paladini, F. Toschi, A. Alabastri, M. Canepa, F. Bisio, *The Journal of Physical Chemistry C* **2019**, *123*, 27 16943.

[60] I. Fratoddi, A. Cartoni, I. Venditti, D. Catone, P. O'Keeffe, A. Paladini, F. Toschi, S. Turchini, F. Sciubba, G. Testa, C. Battocchio, L. Carlini, R. P. Zaccaria, E. Magnano, I. Pis, L. Avaldi, *J. Colloid Interface Sci.* **2018**, *513* 10 .

[61] D. Catone, A. Ciavardini, L. Di Mario, A. Paladini, F. Toschi, A. Cartoni, I. Fratoddi, I. Venditti, A. Alabastri, R. Proietti Zaccaria, P. O'Keeffe, *J. Phys. Chem. Lett.* **2018**, *9*, 17 5002.

[62] F. Toschi, D. Catone, P. O'Keeffe, A. Paladini, S. Turchini, J. Dagar, T. M. Brown, *Adv. Funct. Mater.* **2018**, *28*, 26 1707126.

[63] R. Proietti Zaccaria, F. Bisio, G. Das, G. Maidecchi, M. Caminale, C. Vu, F. De Angelis, E. Di Fabrizio, A. Toma, M. Canepa, *ACS Appl. Mater. Interfaces* **2016**, *8*, 12 8024.

[64] A. Sugawara, K. Mae, *J. Vac. Sci. Technol. B* **2005**, *23*, 2 443.

[65] F. Neubrech, T. Kolb, R. Lovrincic, G. Fahsold, A. Pucci, J. Aizpurua, T. Cornelius, M. Toimil-Molares, R. Neumann, S. Karim, *Appl. Phys. Lett.* **2008**, *89* 253104.

[66] J. Kim, A. Dutta, G. V. Naik, A. J. Giles, F. J. Bezares, C. T. Ellis, J. G. Tischler, A. M. Mahmoud, H. Caglayan, O. J. Glembocki, A. V. Kildishev, J. D. Caldwell, A. Boltasseva, N. Engheta, *Optica* **2016**, *3* 339.

[67] M. Husnik, S. Linden, R. Diehl, J. Niegemann, K. Busch, M. Wegener, *Physical Review Letters* **2012**, *109*, 23 233902.

[68] S. A. Maier, *Plasmonics: Fundamentals and Applications*, Springer Science, **2007**.

[69] P. G. Etchegoin, E. C. Le Ru, M. Meyer, *The Journal of Chemical Physics* **2006**, *125*, 16 164705.

[70] P. B. Johnson, R. W. Christy, *Phys. Rev. B* **1972**, *6* 4370.

[71] E. Carpene, *Physical Review B* **2006**, *74*, 2 024301.

[72] R. Rosei, *Phys. Rev. B* **1974**, *10* 474.

[73] M. Guerrisi, R. Rosei, P. Winsemius, *Phys. Rev. B* **1975**, *12* 557.

[74] A. Marini, M. Conforti, G. Della Valle, H. W. Lee, T. X. Tran, W. Chang, M. A. Schmidt, S. Longhi, P. S. J. Russell, F. Biancalana, *New Journal of Physics* **2013**, *15*, 1 013033.

Table of Contents

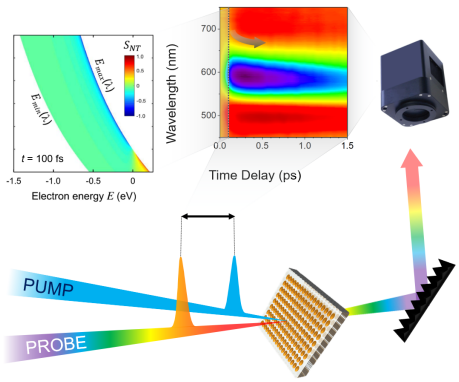

The optical response and ultrafast relaxation of nonthermal electrons generated upon photoexcitation of a 2D array of gold nanoellipsoids have been isolated through the post-processing of femtosecond transient absorbance measurements guided by a reduced semiclassical model. This approach makes it possible to display the intimate correlation between electron energy and probe photon energy on the ultrafast time-scale of electron thermalization.